Inkjet-Printed Flexible mm-Wave Van-Atta Reflectarrays: A Solution for Ultralong-Range Dense Multitag and Multisensing Chipless RFID Implementations for IoT Smart Skins

Jimmy G. D. Hester, *Student Member, IEEE*, and Manos M. Tentzeris, *Fellow, IEEE*

***Abstract*— In this effort, the authors implement the first ultralong-range chipless sensing sticker, by providing more than an order of magnitude increase in reading range, compared with the state of the art. The theoretical advantages of the use of millimeter-wave frequencies for high-performance chipless radio-frequency identification (RFID) sensor implementations are first argued before both a new fully inkjet-printed flexible device, based on the Van-Atta reflectarray structure, as well as a new chipless RFID polarimetric interrogation, and time-frequency data-processing approach is then presented and implemented, for operation in the Ka-band. The array, fully inkjet printed on Kapton HN polyimide, was demonstrated as being robust to variations of interrogation angle (between ±70° from normal), as well as to bending. With its demonstrated range, in excess of 30 m, and its proven adequacy for dense multitag and multisensing implementations in indoor environments, the structure may set the foundation for the emergence of flexible printable low-cost sensing smart skins for the Internet of Things.**

***Index Terms*— Chipless radio frequency identification (RFID), flexible electronics, inkjet printing, Internet of Things (IoT), microstrip antenna arrays, millimeter wave (mm-wave), remote sensing, smart skin.**

I. Introduction

CURRENT technological trends, such as the rise of artificial intelligence and virtual reality, show an evolution toward deepening the connection between the physical world and its digital counterpart. After the creation and exponential rise of world-wide communication networks, during the 20th century, the 21st century has witnessed the development and widespread use of a large range of connected devices, from the smart-phone to the smart-watch. The Internet of Things (IoT) promises to enable all objects with identification, sensing, and communication capabilities, in order to create a dense world-wide network of sensing (gas, strain, location, temperature, and so on) nodes. Nevertheless, this ambitious technological endeavor presents a main challenge: the number of required devices would be extremely large. As a consequence, compatible motes (sensing nodes) must be extremely low cost, power autonomous (no battery), have an environmentally friendly life cycle, and be flexible, in order to be conformably mounted, as smart skins, onto any flexible or curved rigid surfaces. With these requirements in mind, additively manufactured wireless systems and components offer an unequaled appeal. Indeed, additive manufacturing technologies (AMTs) provide an environmentally friendly waste-less approach, where only the required materials are used for the fabrication, while also being compatible with any substrates (flexible or not). Such manufacturing techniques (such as inkjet printing) have been demonstrated [1] for the fabrication of high-performance radio frequency (RF) passive structures, lumped components, and hybrid systems. From a systems perspective, power autonomy requirements have triggered the emergence of, on the one hand, chipped, energy-harvesting-powered motes, which are not fully printable [such as passive RFIDs and wireless identification sensing platform (WISP) architectures], as well as, on the other hand, low cost fully printable chipless RFID systems. Nevertheless, all of these systems (chipless or not) share a common major limitation: short range. Indeed, chipless systems are generally tested in air or in anechoic environments at ranges that do not exceed 1 m [2]–[6], while typical passive RFIDs and WISPs are constrained to ranges of less than 10 m [7]–[11], due to the necessity to harvest the RF energy emitted by the reader, to power themselves. The approach and device presented in this paper describe a way to offer a significant interrogation range increase with respect to these technologies, even in cluttered indoor environments. Current implementations of chipless RFID motes include gas [3], [4], displacement [12], temperature [6], or humidity [2] sensors, and usually rely on one of two distinct mechanisms.

1) Frequency shift of a resonant tag structure that can then be detected by a reader and associated with a sensing event. This technique has the advantage of being quite simple, but is also usually very sensitive to background interference, and therefore ill-suited for real environments [2], [4], [12].
2) Change in the magnitude of the time-resolved response of an ultrawideband tag structure. This technique has produced exciting results, but relies on variations in response magnitude for sensing data extraction.

Manuscript received July 5, 2016; revised September 29, 2016; accepted October 25, 2016. Date of publication November 17, 2016; date of current version December 7, 2016. This work was supported by DTRA. An earlier version of this paper was presented at the IEEE MTT-S International Microwave Symposium, San Francisco, CA, USA, May 22–27, 2016.

The authors are with the Department of Electrical and Computer Engineering, Georgia Institute of Technology, Atlanta, GA 30332 USA (e-mail: jimmy.hester@gatech.edu).

Color versions of one or more of the figures in this paper are available online at http://ieeexplore.ieee.org.

Digital Object Identifier 10.1109/TMTT.2016.2623790

As a consequence, such devices are quite sensitive to interference from nearby scatterers. Furthermore, their required time-resolution necessitates (at the center frequencies of about 5 GHz used in these efforts) bandwidths on the order of 100 %.

In this effort, the authors present a novel approach that takes advantage of a high operating frequency (Ka-band) and of the unique properties of Van-Atta reflectarrays to provide ultralong-range fully chipless wireless sensing, where both time delay and resonant frequency can be used for data extraction and sensor identification. The reported range, in excess of 30 m, represents more than an order of magnitude increase, with regard to that previously reported for the state-of-the-art chipless RFID sensing technologies. It is worth noting that a few efforts have already displayed the use of millimeter wave (mm-wave) frequencies [13], [14], but have not reported a combination of long-range and interrogation-angle-independent sensing, let alone combined time and frequency data extraction capabilities. In this paper, the authors expand upon a previous work [15], which had argued for the potential of printed mm-wave Van-Atta structures for long-range interrogation, and presented a preliminary prototype and approach. Here, this predicted potential is further taken advantage of, and effectively demonstrated. In order to do so, a new processing scheme, allowing for the extraction of both time delay and resonance frequency information, is introduced, and a high-performance reading system assembled. Furthermore, the adequacy of these reported approach and system for ultralong-range multisensor detection in indoor environments is demonstrated. First, the advantages of mm-wave-frequencies-operating Van-Atta reflectarrays are argued, from a theoretical standpoint, in Section II, before the design and inkjet-printing fabrication processes are described, in Section III. The radar cross section (RCS) responses of the array both in flat and bent configurations are presented in Section IV. In Section V, the high-performance data processing scheme is introduced, and used to demonstrate ultralong-range multitag reading capabilities in indoor environments, with range in excess of 30 m. The sensing performance of the sensor and potential of the approach for multisensing implementations is argued in Section VI, before a conclusion is drawn in Section VII.

II. Case for High-Frequency Van-Atta Structures

A. Rise to mm-Wave Frequencies Operation

Whether they are applied to identification and/or sensing purposes, passive chipless RFID structures fundamentally rely on their RCS, and its variation over frequency and time delay, to convey information; the tag operates as a target for a radar-type reader to detect. Nevertheless, the response received in reply to the reader's interrogation, in practical environments, is a combination of several components.

1) The signal produced by an antenna-mode-induced reemission from the tag that encloses the useful information.
2) Interference generated as a consequence of tag scattering-mode-induced reflection.
3) Interference from the background environment.
4) Noise, originating from the environment or reader equipment.

In the absence of nonlinear effects (such as diode-mediated frequency doubling or modulation), all of these components cover one unique frequency, that of the reader. The signal cannot be spectrally isolated, with a given excitation, and can, therefore, easily be drowned in the interference. As a consequence, detection and extraction of the tags responses are one of the main challenges in chipless RFID implementations. For this purpose, three main strategies will be considered in this effort.

1) RCS-based isolation can be used in order to increase the magnitude of the signal, relative to the interference and noise components levels. This can be achieved by, of course, increasing the magnitude of the RCS (making the structure electrically bigger), but also by implementing polarization isolation between signal and interference [5], [14], [16].
2) Frequency and time-delay-based isolation can be applied by discriminating between responses that can, in time and frequency, reasonably be attributed (by filtering) to the tag rather than clutter components.

With these elements in mind, higher frequency operation can be shown to offer tremendous gains in signal detectability for several fundamental and practical reasons. Using $A = ((G\lambda^2)/(4\pi e_a))$ (where A is the physical antenna aperture, G is the antenna gain, λ is the wavelength, and e_a is the antenna aperture efficiency), and the Friis equation, the power received from a monostatic RCS-based reader system, aiming at a tag target, can be expressed as follows:

$$P_r = P_e e_{a,r}^2 e_{a,t}^2 A_r^2 A_t^2 F_t^2(\Theta) \frac{1}{(\lambda R)^4} \tag{1}$$

where R, P_e, P_r, $e_{a,r}$, $e_{a,t}$, A_r, A_t, and $F_t(\theta)$ are, respectively, the reading range, the emitted power, the received power, the aperture efficiencies of the reader antennas (assuming identical antennas), the aperture efficiency of the tag/target/sensor antenna, the physical aperture of the reader antennas, the aperture of the tag, and the radiation pattern of the tag. This can also be rewritten as

$$P_r = P_e e_{a,r}^2 A_r^2 F_t^2(\Theta) \frac{\sigma}{4\pi \lambda^2 R^4} \tag{2}$$

where

$$\sigma = \frac{4\pi e_{a,t}^2 A_t^2}{\lambda^2} \tag{3}$$

is the antenna-mode RCS of the tag. From a tag perspective, these equations lead to several key conclusions. From (2), we can see that the tag is more detectable when the antenna-mode RCS increases. Furthermore, (3) shows us that the RCS of a tag, with a given surface A_t and aperture efficiency $e_{a,t}$, increases with f^2, where $f = (c/\lambda)$ is the frequency. Therefore, all of the other parameters being equal, the detectability of the tag increases with frequency. In addition, (1) allows us to draw a conclusion from a system perspective. Indeed, overall received power varies as $A_r^2 A_t^2 f^4$. Therefore, a system (reader antenna and tag) with given physical dimensions can

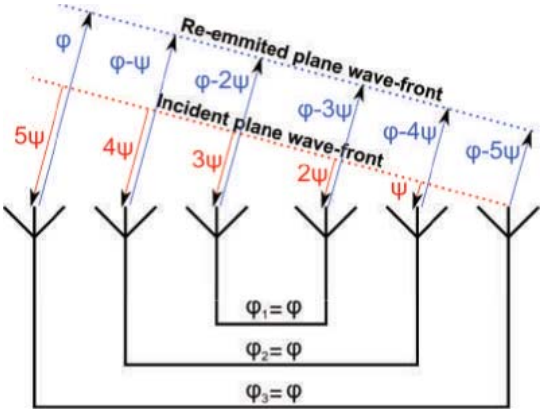

Fig. 1. Van-Atta operation principle schematic.

achieve a much higher detectability, and a system with given detection capability can be made much more compact, as a consequence of an operation frequency increases. These gains can intuitively be understood as the product of higher directivity, leading to a higher power density emitted by the reader to the narrower main beam direction; this is analogous to what can be observed, to a much greater degree, with optical lasers. Furthermore, this also has the effect of decreasing the received level of interference originating from the environment outside of the reader antenna's narrowing main lobe. Nevertheless, high tag-structure directivity can come with a high cost for practical applications, as $F_t(\Theta)$ becomes much less isotropic, and decreases sharply when direction moves away from the tag antenna boresight: the angular tag interrogation range hence becomes much narrower. Nevertheless, this problem can very efficiently be tackled through the use of Van-Atta reflectarray structures.

B. Van-Atta Reflectarray

Van-Atta reflectarrays, whose principle is shown in Fig. 1, are constituted of an array of antennas, interconnected in symmetrical pairs (with reference to an axis or center of symmetry, in the middle of the structure).

Such structures display remarkable properties, if all its connecting lines are of identical electrical lengths. Indeed, such a configuration induces in-phase reemission of the received wave, in the same direction as the impinging reader wave; the boresight of this high gain structure is, therefore, consistently directed toward the reader, regardless of its position, within a wide angular range. This enables the Van-Atta structure with a unique combination of high and theoretically isotropic RCS: the tradeoff between high RCS (for large structures) and isotropic RCS behavior (for small structures) no longer applies. Moreover, cross-polarizing practical implementations of Van-Atta reflectarrays, where the reflected signal is cross polarized with respect to the impinging reader wave, have been demonstrated in the past [16], using two-port rectangular patch arrays. As a consequence, with the considerations of Section II-A in mind, the structure can offer large signal to interference and noise isolation thanks to both high RCS and polarization discrimination, while being detectable from a wide range of directions.

Fig. 2. Inkjet-printed flexible linear antenna array.

III. Inkjet-Printed Van-Atta Reflectarray Design and Fabrication

A. Linear Antenna Array

One of the aspirations of this effort was to develop a low-cost structure that could easily be printed on a flexible, low-cost substrate. As a consequence, a minimalistic single-layer via-less structure was adopted. First, a 1-D microstrip patch antenna array, with two ports (each exciting one of the two cross-polarized degenerate rectangular patch antenna modes), was designed for operation at 30 GHz. The input impedance of each of the patch antennas was $R_{\text{res}} = 178\,\Omega$. With the selected feeding topology, the input impedance of the linear array was, therefore, $R_{\text{in}} = (R_{\text{res}}/N)$, where N is the number of patch antennas. The number of antennas was then chosen as $N = 5$ in order to maximize the overall gain, while utilizing a very manageable characteristic impedance of $(R_{\text{res}}/5) = 39\,\Omega$ for the connecting network lines. A taper from a $50\,\Omega$ to the $39-\Omega$ lines was then added for measurement purposes.

One proof-of-concept prototype of this component was fabricated (Fig. 2) using a Dimatix DMP2830 inkjet-printer and a silver nanoparticle ink from Suntronic, on 5-mil-thick Dupont Kapton HN, a low-cost flexible substrate. In order to provide an increased fabrication accuracy, the effective permittivity (ϵ_{eff}) of microstrip lines, printed on the Kapton substrate, was measured using a two-line phase-shift method, at 30% RH and 25 °C, before the relative dielectric permittivity (ϵ_r) was extracted using the following equation:

$$\epsilon_r = \frac{2\epsilon_{\text{eff}} - 1 + (1 + 12\frac{h}{W})^{-0.5}}{1 + (1 + 12\frac{h}{W})^{-0.5}} \tag{4}$$

where $h = 125\ \mu$m and $W = 0.3$ mm are the thickness of the substrate and the width of the printed lines, respectively. The results (shown in Fig. 3) show good agreement with the datasheet values, and displayed losses in the order of $1.17\,\text{dB}\,\text{cm}^{-1}$ for the lines.

Finally, copper tape was carefully stuck onto the back of the substrate to create a ground plane. The antenna array was then interfaced with end-launch connectors, from Southwest Microwave, and measured using an Anritsu 37369A VNA.

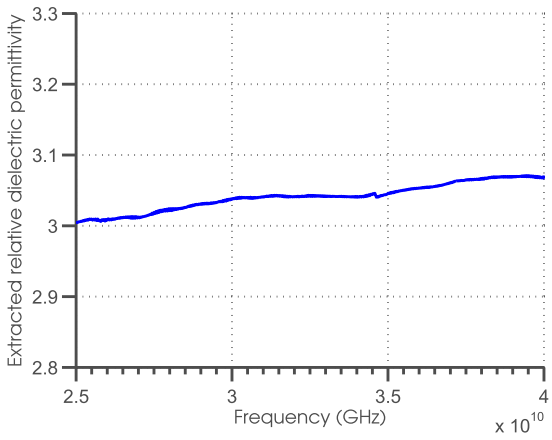

Fig. 3. Dielectric relative permittivity of 5-mil Kapton HN, extracted from the measured data.

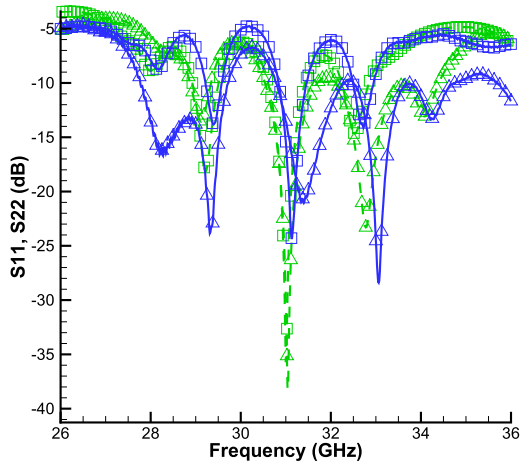

Fig. 4. Measured (blue solid line) and simulated (green dashed line) return loss for the horizontal (triangle) and vertical (rectangle) polarization feeding ports of the series-fed patch antenna array.

Measurement results, as well as its simulation counterparts, are shown in Fig. 4. Measurements feature a very good agreement with simulation, with visible differences on the vertical polarization (with reference to a vertically aligned array), attributed to slight imperfections in the 90 deg microstrip feed turns required for that polarization. That being said, the two ports offer a comatching (two-port being simultaneously matched) of less than −17 dB at 31 GHz, demonstrating, as a consequence, the adequacy of the component for use in the complete Van-Atta array structure.

B. Van-Atta Reflectarray

A Van-Atta reflectarray structure (Fig. 5) was designed and fabricated, by placing five of these series-fed linear antenna arrays side by side, with two of the linear antenna arrays rotated by 180° in order to optimize design compactness, connected in such a way for the reemitted waves to be in-phase in the direction of the impinging interrogation signal (as described in Section II-B), and cross polarized with respect to the impinging wave. This was done by connecting the ports of each linear antenna array to the opposite polarization port of the symmetrical antenna (with respect to the center of the structure), using microstrip transmission lines of controlled

Fig. 5. Inkjet-printed flexible Van-Atta reflectarray prototype, next to a standard "credit card" size RFID tag package.

electrical length. In the configuration chosen here, the linear antenna arrays were flipped with reference to those on the other side, in order to reduce the length of line lengths required to connect the antennas. However, as a consequence, vertical polarization feeds on the left of the array come from the top of the patches, while those on the right are fed from the bottom. This creates π phase shift between the waves received by right-side and left-side antennas, in this polarization, while horizontal polarization ports are consistently fed from the same side. The induced π phase shift was, therefore, compensated for in the connecting network. It should also be noted that this cross-polarizing configuration enables the use of a central, self-connected, linear antenna array, which provides an optimal reemission efficiency, thanks to its minimal connecting line length.

IV. Characterization of the Reflectarray

A. Planar Configuration

Unlike most structures, which offer at least one interfacing waveguide port, reflectarrays can only be characterized by their reflecting properties, or, equivalently, their monostatic (both emitter and receiver in the same position/direction, relative to the tag) or bistatic (emitter and receiver in different directions) RCS. In order to obtain optimal characterization measurements, the reflectarray tag was positioned inside a small anechoic chamber, in order to back it with RF absorbing surfaces, and was interrogated from the outside at a range of 2.5 m. The signal of interest is cross polarized with respect to the emitted signal. For that purpose, two cross-polarized antennas were connected on both ports of the VNA. In the case of an anechoic environment, the measured response is comprised of three major components

$$y = G[s + r_{g,\text{X-pol}} + 2 * I_{\text{X-pol}} * r_{g,\text{co-pol}}] \tag{5}$$

where s is the cross-polarized array response, $I_{\text{X-pol}}$ is the the cross-polarization isolation of the used antennas (assuming identical receiving and emitting antennas), G is the antennas gain, and $r_{g,\text{X-pol}}$ and $r_{g,\text{co-pol}}$ are the cross polarized and copolarized responses of the rectangular metallic plane that forms the ground of the device. The factor 2 in front of the

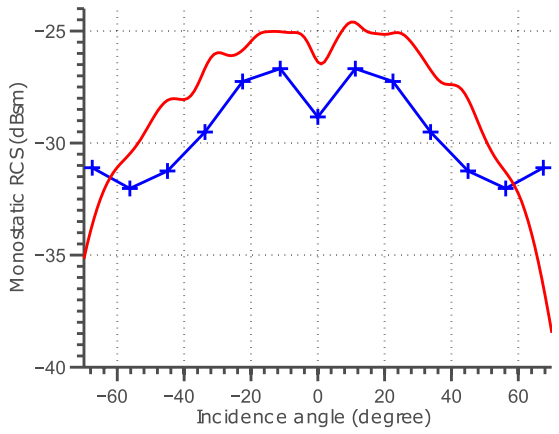

Fig. 6. Measured (blue +) and simulated (red solid line) monostatic RCS of the Van-Atta reflectarray.

isolated signal accounts for the main polarization emission signal response received on the secondary polarization of the receiving antenna, as well as for the secondary-polarization signal radiated by the emitting antenna received on the main polarization of the receiving antenna. The cross-polarized RCS of a metallic plane is generally far smaller than the RCS response of the array. On the other hand, the same cannot be said about its copolarized response. The copolarized maximum RCS (in broadsight) of a rectangular ground plane can be approximated by

$$r_{\text{ground, X-pol}} = 4\pi \left(\frac{WL}{\lambda}\right)^2 \tag{6}$$

where W and L are the width and length of the rectangular metal plane, respectively. Given the device dimensions (5 cm × 5 cm), this signal can, here, be on the order of −1 dBsm, which, as we will see, is quite significant. Therefore, high cross-polarization isolation of the antennas used for the measurement is paramount. As a consequence, two 19-dB gain conical horn antennas with 40-dB cross-polarization isolation were used for the reflectarray's interrogation. A 20-dB gain amplifier was added on the emission channel, to increase signal level, and the monostatic RCS of the tag/array was measured for different angles of incidence, with respect to normal. Finally, a 12-in sphere was measured in the same configuration, to establish a reference RCS. It should be noted that the 2.5-m range was chosen in order to provide high measured signal responses, while allowing the sphere to fit entirely into the reader antennas main lobes, for adequate calibration. The measured RCS of the reflectarray as well as its simulation counterpart are shown in Fig. 6. The measured and simulated (using HFSS) results show a very good agreement, and both display the expected Van-Atta behavior. Indeed, the RCS of the tag only changes by, at most, 10 dB over a range of 140° around boresight, and the structure displays both a high (up to −26 dBsm) and interrogation-angle-robust RCSs.

B. Curved Configurations

As a flexible conformable mm-wave reflectarray, variations of the tag response with bending can be of concern. The reflectarray was, therefore, characterized in various bending configurations, starting with uniform bending around cylinders of various radii with its axis parallel to the linear antenna arrays of the tag.

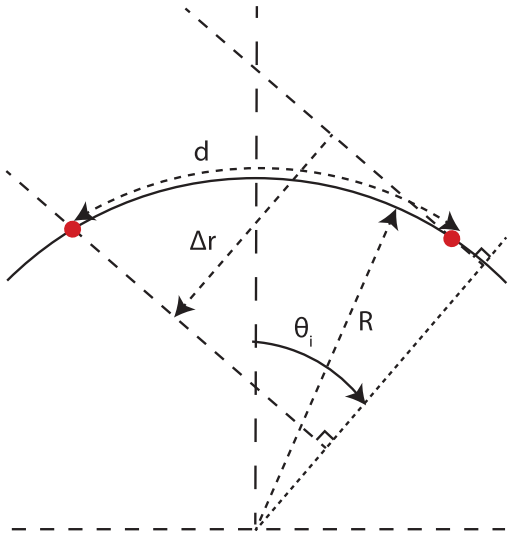

Fig. 7. Geometrical model considered for curvature-induced phase-shift calculation.

For a parallel curvature axes, the observed RCS variations, shown in Fig. 7, are quite modest, and are comprised of two effects.

1) A slight reduction in the range of Van-Atta retrodirective behavior, with a sharper decrease of the response at angles further away from boresight. The curvature detunes the reflectarray by adding an additional phase shift in the waves received by complementary antennas (with reference to the center of the array). Indeed, by considering point-located antennas, and an array covering no more than a 180° angle of the cylinder's surface (as shown in Fig. 7), it can be found that the difference in path lengths, with an impinging wave arriving with an angle θ_i from normal, can be expressed as

$$\Delta r = \frac{4\pi R}{\lambda} \sin\left(\frac{d}{2R}\right) \sin(\theta_i) \tag{7}$$

where R is the curvature radius and d is the distance (on the planar array) between the connected antenna pairs. As a consequence, the phase difference introduced by the curvature (with respect to the flat case) can be expressed as

$$\Delta\phi = \left(-\frac{2\pi\,\Delta r}{\lambda} + \frac{2\pi d}{\lambda}\right) \sin(\theta_i) \tag{8}$$

$$= \frac{2\pi}{\lambda}\left(d - 2R\sin\left(\frac{d}{2R}\right)\right) \sin(\theta_i) \tag{9}$$

where λ is the wavelength. In the worst case considered here ($R = 7.62$ cm) for the outer antenna pair ($d \approx 5\lambda = 5$ cm), the maximum phase shift (at $\theta_i = 70°$) is equal to $\Delta\phi = 0.168\pi$. This value is quite negligible, as such a small value does not induce a large change in the array factor, and is also far larger than that introduced for closer pairs and at lower incidence angles.

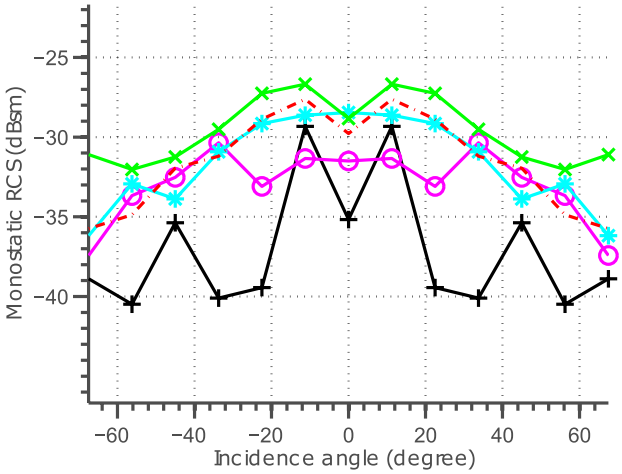

Fig. 8. Measured RCS for flat (green x), parallel-axis-curved with radii of 5 (red dashed point), 4 (blue stars), and 3 in (magenta circles), and horizontal-axis-curved with 5-in radius (black +).

2) A reduction in the overall RCS. This can be explained as a consequence of the angle-dependent gain of the patch antennas that form the reflectarray. The incidence angle direction moves away from the patch antennas boresights as the curvature increases, which contributes in flattening out the RCS response, from the center. This is the main effect observed in Fig. 8.

In a second experiment, the antenna array was curved on cylinders with axes perpendicular to the linear antenna arrays. The results, shown on Fig. 8, show a remarkable difference with that taken with a parallel curvature axis orientation, and the overall RCS is reduced by a significant amount, and displays a quite irregular shape. Measurements with such curvature axes also stand out by their particularly high interference floor. This is caused not by array structure itself, but by its ground plane. Indeed, when curved with an axis on the plane formed by the tag and the interrogation antennas, the currents created on the curved surface of the ground conductor create a large cross-polarized response, which then becomes significant enough to nonnegligibly interfere with the measurement capability of the system. That being said, this effect is general to all grounded polarity-rotating designs, and might be resolvable through the use of ground edge patterning techniques.

V. Optimal Signal Processing for Long-Range Multitag Interrogation

In addition to a high-performance physical tag structure, which provides an unequaled combination of low cost, flexibility, cross-polarized response, and high and isotropic RCS at mm-wave frequencies, high frequency operation enables the implementation of optimal reading schemes, in order to provide high-resolution time-frequency multitag long-range detectability.

A. Data Processing Scheme for High-Performance Range and Resonant-Frequency-Based Identification

A high-performance and computationally modest matched-windowing spectrogram approach, allowing for adequate signal extraction without the need for environmental calibration, was chosen. A step-by-step flowchart of the entire data processing scheme can be seen in Fig. 9. It should be noted that this process does not require a measurement of the background, as is done in [6], for example.

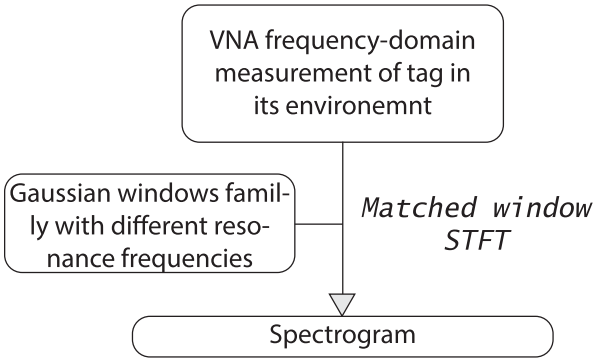

Fig. 9. Processing steps of the measured data for high-performance resonant frequency and range extraction.

For high-performance signal extraction in both time and frequency domains, a short time Fourier transform (STFT), where the windowing function is identical to the expected signal (as described in [17]), was used to process the received response. In the experiments described later in this paper, the response was measured in frequency domain, using a VNA, as S_{21} from the emitting antenna to the receiving antenna. n_t, n_f, k_t, and k_f used in this section are integer indices that span $[\![1; N]\!]$, where N is the number of measured frequency points. The frequency-response S_{21} complex data vector $r(k_f)$, exported from the measurement equipment, was then processed through an inverse fast Fourier transform (IFFT) to extract the time-domain response of the system $r(k_t) = \text{IFFT}[r(k_f)]$. Through the IFFT, N discrete frequency points in the $(f_{\min}, f_{\max})$ range, with steps Δf, map to a set of time points in the $(t_{\min} = 0 and t_{\max} = N\Delta t)$ range with increment $\Delta t = (1/N\Delta f)$. An STFT can then be applied in the following way:

$$\text{STFT}(n_t, n_f) = \sum_{k_t=0}^{N} r^*(k_t) w(k_t - n_t, n_f) e^{-2i\pi n_f k_t} \quad (10)$$

where $w(k_t, l_f)$ is the time-frequency response of the applied window, $\text{STFT}(n_t, n_f)$ is the output signal, and $r(k_t)$ is the measured data, in time-frequency-domain, which may be expressed as

$$r(k_t) = s(k_t) + i(k_t) + n(k_t) \quad (11)$$

where $s(k_t)$ is the Van-Atta response signal, $i(k_t)$ is the interference, and $n(k_t)$ is the noise. In the cases of the experiments described in this paper, a complex signal was measured in frequency domain, using a VNA. While the magnitude of the signal encloses the frequency information, its phase (though FT) allows for the retrieval of time-delay information, a feature that will be exploited later on. In this configuration, optimal detection can be achieved through the use of a window whose shape is that of the expected signal, $s(k_t)$. In our configuration, we assume a constant relative bandwidth for the Van-Atta array, regardless of its resonance frequency.

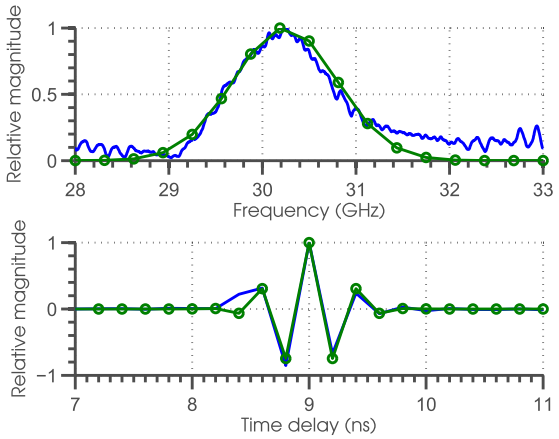

Fig. 10. Measured array response (blue) and fitted Gaussian used as matched window (green circles), plotted in time and frequency domains.

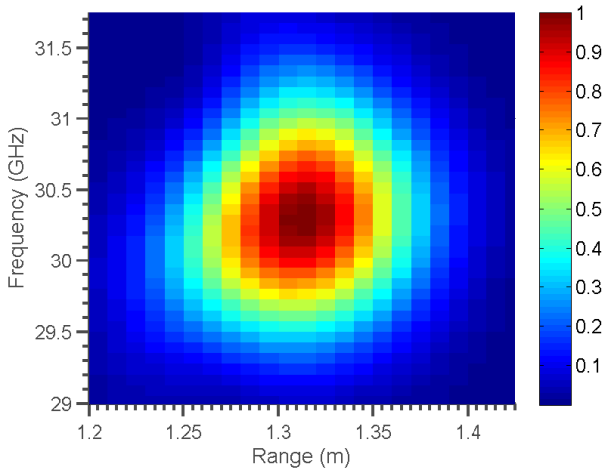

Fig. 11. Spectrogram of the measurement in the configuration, as shown in Fig. 10.

As a consequence, the absolute bandwidth of the received signal $s(k_t)$ depends on the (unknown) resonance frequency of the array. Therefore, contrary to usual STFT implementations, the window is made frequency-dependent, and the absolute bandwidth of the filtering window is changed for each different center frequency.

In order to find the shape of this optimal window, the intrinsic response of the array, isolated from the environmental interference found in real-world configurations, was characterized. In order to do so, the frequency response of the array was measured in the anechoic chamber, at close range (about 1 m), for better accuracy, and fitted with a Gaussian function in frequency domain (shown in Fig. 10, where the time origin was shifted to fit the time delay of the measurement), using least square optimization over a range of twice the frequency width at half maximum (FWHM). A family of such functions, with different center frequencies $[f_0(n_f)]$ and assuming identical resonance relative FWHM $[\text{FWHM}_r = (\text{FWHM}/f_0(n_f)) = 0.0417]$, and identical power, was then created

$$W(k_f, n_f) = \frac{1}{\sqrt[4]{\sigma(n_f)^2\pi}} e^{\frac{-\left(f(k_f)-f_0(n_f)\right)^2}{2\sigma^2(l_f)}} \tag{12}$$

where

$$\sigma(n_f) = \frac{f_0(n_f) * \text{FWHM}_r}{2\sqrt{2\ln 2}} \tag{13}$$

where $f_0(n_f) = f_{\min} + n_f \Delta f$ and $f_0(k_f) = f_{\min} + k_f \Delta f$.

The time-domain response of the window was then obtained through IFFT, with

$$w(k_t, n_f) = \text{IFFT}_{k_f}[W(k_f, n_f)] \tag{14}$$

where "IFFT_{k_f}" is the IFFT operation, applied along the dimension of indice k_f.

Then, the summation of (10) was applied, before the spectrogram was obtained from the squared magnitude of the STFT

$$S(n_t, n_f) = |\text{STFT}(n_t, n_f)|^2. \tag{15}$$

The result of such a process, applied to the measurement data shown in Fig. 10, is displayed in Fig. 11. On the following spectrograms, the response is expressed as a function of range, where the range is extracted from the round trip time $R = (ct/2)$, where c is the speed of light in vacuum and t is the time delay of the vector point. It is apparent that this processing scheme enables the extraction of both time delay (range) and frequency information from the tag.

B. Multitag Detection

One of the main advantages of the use of mm-wave frequencies, along with the presented processing scheme, is that both high relative frequency and high absolute range resolutions can be achieved. Indeed, from a time/frequency resonance detection perspective, the frequency (Δf) and time (Δt) resolutions of a data set (where frequency and time data are related by FFT and IFFT) are dependent according to

$$\frac{1}{N} = \Delta t \Delta f \tag{16}$$

$$= \Delta t \, (\Delta f)_r \, f_0 \tag{17}$$

where N is the number of measured data points, f_0 is the center frequency of interest, and $(\Delta f)_r$ is the relative frequency resolution. For a given $(\Delta f)_r$ (constant for frequency-scaled identical structures) and for a given number of samples, time resolution increases by an f_0 factor. That being said, this process also opens broad opportunities for multisensor and multisensing configurations. Indeed, for a usual Gaussian frequency tag response, the measured frequency (σ_f) and time (σ_t) half-power bandwidth (HPBW) of the FT-related responses are constrained by

$$\frac{4\ln 2}{\pi} \leq \sigma_t \sigma_f \tag{18}$$

$$\leq \sigma_t (\sigma_f)_r f_0 \tag{19}$$

where $(\sigma_f)_r$ is the relative HPBW. As a practical consequence, the theoretical minimum delay and/or relative frequency differences required in order to differentiate two tags, adjacent in resonance frequency and/or delay, decrease linearly with increased operation frequency. In the measurement shown on Fig. 11, these values were measured as $\sigma_t = 0.67$ ns and $\sigma_f = 1.43$ GHz, with $\sigma_t \sigma_f = 1.08(4\ln 2/\pi)$, displaying only a factor 1.08 from theoretical ideality.

Fig. 12. Target measurement configuration for dual-tag detection demonstration.

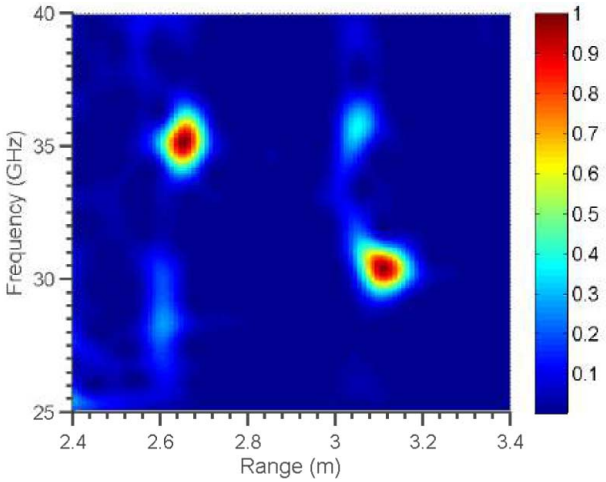

Fig. 13. Spectrogram of the measurement in the multitag configuration, as shown in Fig. 12.

In order to demonstrate the multitag detection capability of this approach, a second tag, with a 35-GHz resonant frequency was fabricated. Both tags were then set side-by-side (Fig. 12), and interrogated with the same configuration, as described in Section IV. The result of this test can be seen in Fig. 13.

As expected, both tags are extremely well resolved in time, as well as in resonant frequency. This demonstrates the capability of the system for high-density range and/or frequency divided multitag implementations. Unlike other methods, this scheme allows for the individual detection of several tags with identical or otherwise unresolvable resonance frequencies, but positioned at different ranges, either introduced by their different locations or by the use of delay lines. The same reasoning, of course, also applies to tags with at identical ranges but different resonance frequencies. As such, the identity of each tag is encoded in a combination of its resonance frequency, its range, and its direction (enabled by the high reader antenna directivity). Within the popular bit-by-bit encoding scheme [18], each Van-Atta array would encode 1 b of information. However, while bits are usually spread only over the frequency spectrum, the presented Van-Atta implementation allows for their distribution over both time delay and frequency domains. An assembly of N Van-Atta array tags would, therefore, be able to encode N bits, where each bit is associated with a unique (t_i, f_i) time-delay frequency couple.

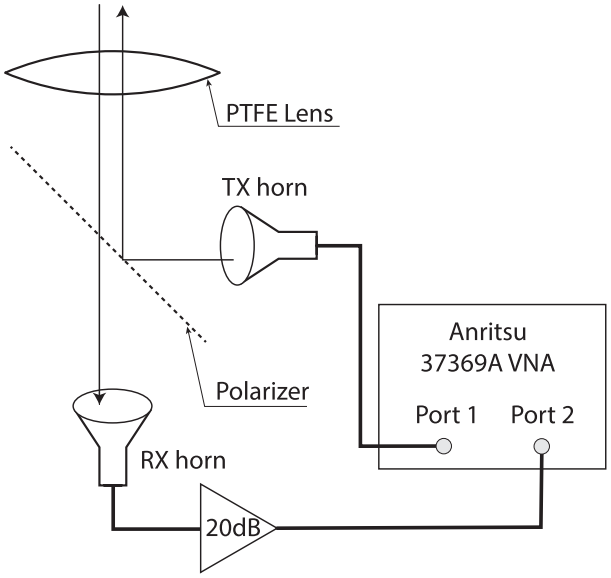

Fig. 14. Schematic of the reading system used for the measurement, as shown in Fig. 15.

C. Ultralong-Range Detection

As extensively argued in Section II, one of the main appeals of the proposed device and approach is the high detectability and, incidentally, ultralong expected range. In order to test this promise, a high-performance antenna system, comprised of the same conical horn antennas used for the previously reported measurement, a 300-mm-diameter dielectric lens (for high directivity), and an inkjet-printed mm-wave polarizer, was assembled, as shown in Fig. 14.

An amplifier with a gain 20 dB was added on the receiving channel, in order to increase the signal level. The output power of the Anritsu 37369A VNA used for the measurement was set at -10 dBm which, with a theoretical maximum gain of the lens antenna of $G_{\max} = ((4\pi^2 R_{\text{lens}}^2)/\lambda^2) = 39.48$ dB (where R is the radius of the lens), keeps the equivalent isotropic radiated power under 1 W. This reading system was then set-up indoors, in a real environment, and aimed at a Van-Atta target, at a range of 30.5 m (confirmed with a laser ranging system), in the configuration, as shown in Fig. 15, with a link budget, calculated from (2), of

$$P_r = P_e e_{a,r}^2 A_r^2 \frac{\sigma}{4\pi\lambda^2 R^4} \tag{20}$$

$$= -108\,\text{dBm} \tag{21}$$

where $P_e = -10$ dBm, $A_r = \pi R_{\text{lens}}^2 = -11.5$ dBsm (where $R_{\text{lens}} = 15.24$ cm), $\sigma = -27$ dBsm, $\lambda = 1$ cm, $R = 30.5$ m, and $e_{a,r} = -9$ dB. It should be noted that, at 30 GHz, the atmospheric attenuation is on the order of 0.1 dB km^{-1} [19], and is, therefore, not included in the calculation. The received signal is then amplified by 20 dB before reaching the VNA.

Fig. 15. Measurement configuration at an interrogation range of 30.5 m.

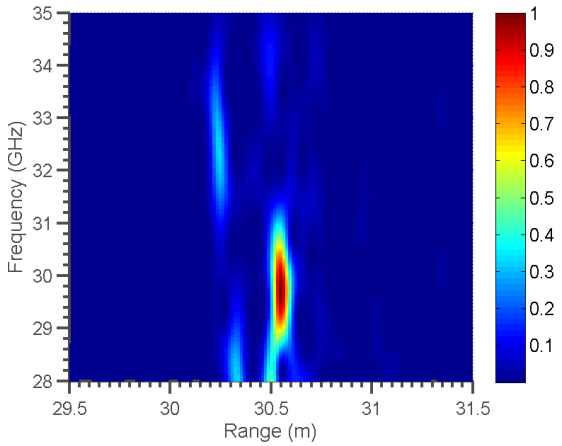

Fig. 16. Spectrogram of the measurement in the long-range configuration, as shown in Fig. 15.

The measured data was then processed according to the scheme displayed in Fig. 9, and described in Section V-A, the output of which can be seen in Fig. 16. Here, the peak is also easily extracted, and has HPBWs of $\sigma_t = 0.5\,\text{ns}$ $\sigma_f = 1.9\,\text{GHz}$. The lower signal level, noisier and more interference-prone environment contributed toward widening the frequency spread of the detected signal. That being said, the signal is still extremely resolvable; this suggests even longer range capabilities. This demonstrated range represents an improvement of at least an order of magnitude upon that of the state-of-the-art chipless RFID devices and approaches.

VI. Toward Low-Cost Multiparameter Multisensor Constellations

In Section V, the array tag, interrogated with a high-performance reading system, and processed with optimal signal extraction methods, demonstrated its capability for long-range high-density multidevice detection implementations in indoor environments. The proposed data processing scheme also allowed for the extraction of both range and resonance frequency information, with high accuracy. As it is, the system has already been demonstrated as capable of being applicable

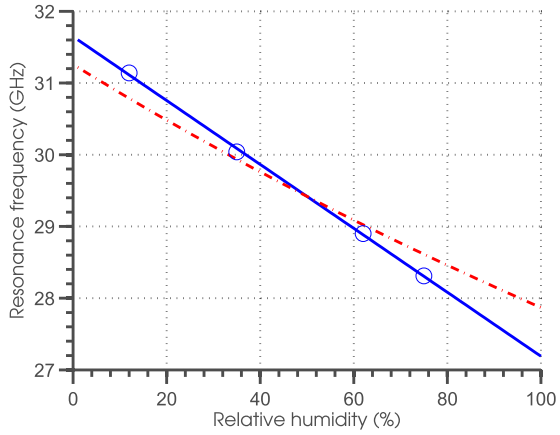

Fig. 17. Plot of the measured resonance frequency of the inkjet-printed Van-Atta reflectarray as a function of the ambient humidity level (circles), its linear fit (blue line), and theoretical model prediction (red dashed-dotted line).

to range finding, as well as to time delay and resonant-frequency-based tag identification. The capability of interrogating several tags, from a wide range of angles, also enables it with angle measurement capabilities, where the measured delay between two tags, placed on a surface at know distances from each other, could be associated with an interrogation angle. Nevertheless, one of the main appeals of both time and resonant-frequency extraction lies in the potential implementation of high densities of resonance-frequency-shift-based chemical sensors. As presented in [15], the proposed array can also act as a humidity sensor, thanks to the relative humidity (RH)-dependent dielectric constant of the utilized Kapton HN substrate. In the real-environment configuration described in [15], the shift of resonance frequency with RH, reproduced on Fig. 17, had been measured and displayed remarkable linearity. The Kapton datasheet, from Dupont, describes the following law for the humidity-dependent permittivity (at 23 °C, for an unspecified frequency):

$$\epsilon_r(\text{RH}) = 3 + 0.008\text{RH} \tag{22}$$

where RH is the relative humidity level, in %. Assuming an array resonant-frequency variation proportional to that of its constituting patch antennas ($\propto (1/(\epsilon_r)^{(1/2)})$), the theoretical response of the array was plotted against the measured data (Fig. 17). Both theoretical and measured responses show good agreement, therefore confirming that the main sensing mechanism relies on the humidity-dependent permittivity of the Kapton substrate. Thanks to its compatibility with AMTs, such as inkjet printing, the proposed sensor design could readily be printed onto other chemisensitive substrates, to provide multisensor multianalyte long-range detection capabilities.

Finally, it should be noted that the grounded design of the sensor offers two significant advantages for permittivity-based detection.

1) The ground completely isolates the behavior of the sensor from potential supporting material influence. As a consequence, such sensors do not suffer from the typical detuning that can be observed with nongrounded structures.

2) The electromagnetic field inside the structure is mostly confined within the substrate. Therefore, any change of its material permittivity has a high impact on the resonant frequency of the sensor tag. Indeed, this configuration displays a relative sensitivity to humidity $((1/f_0)(\Delta f/\Delta \mathrm{RH}) = 1.41)$ that is almost 1 order of magnitude higher than of the state of the art of Kapton-based wireless humidity sensors [11].

VII. Conclusion

In this paper, the authors introduced a new approach for chipless RFID and sensing, based upon the advantages of mm-wave operation for ultralong-range multisensor chipless RFID implementations, providing an increase in reading range by more than an order of magnitude, compared with the state of the art. The printed Van-Atta reflectarray structure, thanks to its unique properties, also allows reading from a large set of interrogation angles, while providing a large RCS response. It is the hope of the authors that the overall approach and data processing technique reported in this effort, allowing the high-performance extraction of both time delay and resonant-frequency information, for ultralong-range interrogation, will trigger a growing interest, for mm-wave frequency chipless RFID and sensors technologies, and their development. A combination of our approach with previously reported SAR [14] or FMCW [20] methods could, for example, provide full 3-D localization, along with resonance frequency extraction. Finally, the device, with its form factor, is the first demonstration of what could essentially be described as a fully printable (and roll-to-roll process compatible) ultralong-range sensing sticker ("Sensticker"). As such, the reported printed Van-Atta chipless reflectarray sensor may well set the foundation for the emergence of the first commercial generation of ultralong-range, fully printable, chipless, flexible, low cost, wireless sensors for applications in ubiquitous smart skins and the IoT multisensing topologies.

References

[1] J. G. Hester *et al.*, "Additively manufactured nanotechnology and origami-enabled flexible microwave electronics," *Proc. IEEE*, vol. 103, no. 4, pp. 583–606, Apr. 2015.

[2] E. M. Amin, M. S. Bhuiyan, N. C. Karmakar, and B. Winther-Jensen, "Development of a low cost printable chipless RFID humidity sensor," *IEEE Sensors J.*, vol. 14, no. 1, pp. 140–149, Jan. 2014.

[3] S. Shrestha, M. Balachandran, M. Agarwal, V. V. Phoha, and K. Varahramyan, "A chipless RFID sensor system for cyber centric monitoring applications," *IEEE Trans. Microw. Theory Techn.*, vol. 57, no. 5, pp. 1303–1309, May 2009.

[4] L. Yang, R. Zhang, D. Staiculescu, C. P. Wong, and M. M. Tentzeris, "A novel conformal RFID-enabled module utilizing inkjet-printed antennas and carbon nanotubes for gas-detection applications," *IEEE Antennas Wireless Propag. Lett.*, vol. 8, pp. 653–656, 2009.

[5] B. Kubina, C. Mandel, M. Schüßler, M. Sazegar, and R. Jakoby, "A wireless chipless temperature sensor utilizing an orthogonal polarized backscatter scheme," in *Proc. 42nd Eur. Microw. Conf. (EuMC)*, Oct. 2012, pp. 61–64.

[6] D. Girbau, A. Ramos, A. Lazaro, S. Rima, and R. Villarino, "Passive wireless temperature sensor based on time-coded UWB chipless RFID tags," *IEEE Trans. Microw. Theory Techn.*, vol. 60, no. 11, pp. 3623–3632, Nov. 2012.

[7] C. Occhiuzzi, A. Rida, G. Marrocco, and M. Tentzeris, "RFID passive gas sensor integrating carbon nanotubes," *IEEE Trans. Microw. Theory Techn.*, vol. 59, no. 10, pp. 2674–2684, Oct. 2011.

[8] S. Merilampi, T. Björninen, L. Ukkonen, P. Ruuskanen, and L. Sydänheimo, "Embedded wireless strain sensors based on printed RFID tag," *Sensor Rev.*, vol. 31, no. 1, pp. 32–40, 2011.

[9] S. Kim, Y. Kawahara, A. Georgiadis, A. Collado, and M. M. Tentzeris, "Low-cost inkjet-printed fully passive RFID tags for calibration-free capacitive/haptic sensor applications," *IEEE Sensors J.*, vol. 15, no. 6, pp. 3135–3145, Jun. 2015.

[10] J. Gao, J. Siden, H.-E. Nilsson, and M. Gulliksson, "Printed humidity sensor with memory functionality for passive RFID tags," *IEEE Sensors J.*, vol. 13, no. 5, pp. 1824–1834, May 2013.

[11] J. Virtanen, L. Ukkonen, T. Björninen, A. Z. Elsherbeni, and L. Sydänheimo, "Inkjet-printed humidity sensor for passive UHF RFID systems," *IEEE Trans. Instrum. Meas.*, vol. 60, no. 8, pp. 2768–2777, Aug. 2011.

[12] C. Mandel, B. Kubina, M. Schüßler, and R. Jakoby, "Passive chipless wireless sensor for two-dimensional displacement measurement," in *Proc. 41st Eur. Microw. Conf. (EuMC)*, Oct. 2011, pp. 79–82.

[13] H. Aubert *et al.*, "Wireless sensing and identification based on radar cross section variability measurement of passive electromagnetic sensors," *Ann. Telecommun.-Annales Télécommun.*, vol. 68, no. 7, pp. 425–435, Aug. 2013.

[14] M. Zomorrodi and N. C. Karmakar, "Novel MIMO-based technique for em-imaging of chipless RFID," in *IEEE MTT-S Int. Microw. Symp. Dig.*, May 2015, pp. 1–4.

[15] J. G. D. Hester and M. M. Tentzeris, "Inkjet-printed van-atta reflectarray sensors: A new paradigm for long-range chipless low cost ubiquitous smart skin sensors of the Internet of Things," in *IEEE MTT-S Int. Microw. Symp. Dig.*, May 2016, pp. 1–4.

[16] J. A. Vitaz, A. M. Buerkle, M. Sallin, and K. Sarabandi, "Enhanced detection of on-metal retro-reflective tags in cluttered environments using a polarimetric technique," *IEEE Trans. Antennas Propag.*, vol. 60, no. 8, pp. 3727–3735, Aug. 2012.

[17] D. L. Jones and T. W. Parks, "A resolution comparison of several time-frequency representations," *IEEE Trans. Signal Process.*, vol. 40, no. 2, pp. 413–420, Feb. 1992.

[18] I. Preradovic, I. Balbin, N. C. Karmakar, and G. F. Swiegers, "Multiresonator-based chipless RFID system for low-cost item tracking," *IEEE Trans. Microw. Theory Techn.*, vol. 57, no. 5, pp. 1411–1419, May 2009.

[19] *Attenuation by Atmospheric Gases*, document ITU-R P.676, vol. 8, I. Recommendation, 2009.

[20] D. Henry, H. Aubert, and P. Pons, "3D scanning and sensing technique for the detection and remote reading of a passive temperature sensor," in *IEEE MTT-S Int. Microw. Symp. Dig.*, May 2016, pp. 1–4.

Jimmy G. D. Hester (S'14) received the Degree in fundamental chemistry, math, and physics, and the graduate degree and the M.S. degree in electrical and signal processing engineering, majoring in radio frequency electronics, from the INP Toulouse, ENSEEIHT, Toulouse, France, in 2012 and 2014, respectively, and the M.S. degree in electrical and computer engineering from the Georgia Institute of Technology, Atlanta, GA, USA, in 2014, where he is currently pursuing the Ph.D. degree in electrical and computer engineering.

He is currently a Research Assistant with the ATHENA Group, Georgia Institute of Technology. His current research interests include the interface between radio frequency engineering and material science, in the form of flexible electronics technologies and nanotechnologies. He has been developing solutions for the use of carbon nanomaterials and optimized RF structures toward the implementation of inkjet-printed flexible low cost ubiquitous gas sensors for Internet of Things and Smart Skin applications. His work covers the entire development process, from the development of inkjet inks, improvement of fabrication methods, sensor component design, high frequency characterization and environmental testing to the design, simulation, and fabrication of the RF system embedding the sensor.

Manos M. Tentzeris (S'89–M'92–SM'03–F'10) received the Diploma (*magna cum laude*) degree in electrical and computer engineering from the National Technical University of Athens, Athens, Greece, and the M.S. and Ph.D. degrees in electrical engineering and computer science from the University of Michigan, Ann Arbor, MI, USA.

He was a Visiting Professor with the Technical University of Munich, Munich, Germany, in 2002, a Visiting Professor with GTRI-Ireland, Athlone, Ireland, in 2009, and a Visiting Professor with LAAS-CNRS, Toulouse, France, in 2010. He has given over 100 invited talks to various universities and companies all over the world. He was the Head of the ATHENA Research Group (20 researchers). He was with the Georgia Institute of Technology, Atlanta, GA, USA, where he has served as the Head of the GT-ECE Electromagnetics Technical Interest Group, the Associate Director for RFID/Sensors Research with the Georgia Electronic Design Center, the Associate Director of the RF Research with the Georgia Tech NSF-Packaging Research Center, and the RF Alliance Leader. He is currently a Ken Byers Professor in flexible electronics with the School of Electrical and Computer Engineering, Georgia Institute of Technology. He has authored over 620 papers in refereed journals and conference proceedings, five books, and 25 book chapters. He has helped develop academic programs in 3-D/inkjet-printed RF electronics and modules, flexible electronics, origami and morphing electromagnetics, highly integrated/multilayer packaging for RF and wireless applications using ceramic and organic flexible materials, paper-based RFID's and sensors, wireless sensors and biosensors, wearable electronics, green electronics, energy harvesting and wireless power transfer, nanotechnology applications in RF, microwave MEM's, SOP-integrated (UWB, multiband, mmW, and conformal) antennas.

Dr. Tentzeris is a member of the URSI-Commission D, a member of the MTT-15 Committee, an associate member of the EuMA, a Fellow of the Electromagnetic Academy, and a member of the Technical Chamber of Greece. He served as one of the IEEE MTT-S Distinguished Microwave Lecturers from 2010 to 2012 and the IEEE CRFID Distinguished Lecturers. He was a recipient/corecipient of the 2015 IET Microwaves, Antennas and Propagation Premium Award, the 2014 Georgia Tech ECE Distinguished Faculty Achievement Award, the 2014 IEEE RFID-TA Best Student Paper Award, the 2013 IET Microwaves, Antennas and Propagation Premium Award, the 2012 FiDiPro Award in Finland, the iCMG Architecture Award of Excellence, the 2010 IEEE Antennas and Propagation Society Piergiorgio L. E. Uslenghi Letters Prize Paper Award, the 2011 International Workshop on Structural Health Monitoring Best Student Paper Award, the 2010 Georgia Tech Senior Faculty Outstanding Undergraduate Research Mentor Award, the 2009 IEEE TRANSACTIONS ON COMPONENTS AND PACKAGING TECHNOLOGIES Best Paper Award, the 2009 E.T.S.Walton Award from the Irish Science Foundation, the 2007 IEEE APS Symposium Best Student Paper Award, the 2007 IEEE IMS Third Best Student Paper Award, the 2007 ISAP 2007 Poster Presentation Award, the 2006 IEEE MTT Outstanding Young Engineer Award, the 2006 Asian-Pacific Microwave Conference Award, the 2004 IEEE TRANSACTIONS ON ADVANCED PACKAGING Commendable Paper Award, the 2003 NASA Godfrey Art Anzic Collaborative Distinguished Publication Award, the 2003 IBC International Educator of the Year Award, the 2003 IEEE CPMT Outstanding Young Engineer Award, the 2002 International Conference on Microwave and Millimeter-Wave Technology Best Paper Award, Beijing, China, the 2002 Georgia Tech-ECE Outstanding Junior Faculty Award, the 2001 ACES Conference Best Paper Award and the 2000 NSF CAREER Award, and the 1997 Best Paper Award of the International Hybrid Microelectronics and Packaging Society. He was the TPC Chair of the IEEE IMS 2008 Symposium and the Chair of the 2005 IEEE CEM-TD Workshop. He is the Vice-Chair of the RF Technical Committee (TC16) of the IEEE CPMT Society. He is the Founder and the Chair of the RFID Technical Committee (TC24) of the IEEE MTT Society and the Secretary/Treasurer of the IEEE C-RFID. He has served as an Associate Editor of the IEEE TRANSACTIONS ON MICROWAVE THEORY AND TECHNIQUES, the IEEE TRANSACTIONS ON ADVANCED PACKAGING, and the *International Journal on Antennas and Propagation*.